Journal of Inorganic and Organometallic Polymers and Materials (2019) 29:827–840
https://doi.org/10.1007/s10904-018-01057-0

MnO_2 Nanoparticles Supported on Porous Al_2O_3 Substrate for Wastewater Treatment: Synergy of Adsorption, Oxidation, and Photocatalysis

Sherif Elbasuney[1] · Mohamed A. Elsayed[2] · Sherif F. Mostafa[2] · Waleed F. Khalil[2]

Received: 24 September 2018 / Accepted: 13 December 2018 / Published online: 7 January 2019

Abstract
Even though photocatalyst nanoparticles can offer effective degradation of organic pollutants, this can stimulate another pollution problem related to contamination with nanoparticle themselves. Furthermore particle aggregation could cause reduction of interfacial surface area and photocatalytic efficiency. One effective approach for wastewater treatment is superimposing photocatalyst on a high surface area porous support. MnO_2 has attracted attention as its electronic structure is semiconducting. The d–d electronic transitions can take place under illumination as the d-orbitals are not completely occupied. This study reports on a new approach of sustainable fabrication of mono-dispersed MnO_2 particles (20 nm average particle size) with a constant product quality using hydrothermal synthesis procedures. TEM and SEM procedures were utilized to study the particle size and morphological structure of the prepared MnO_2 particles. While the crystalline phase was measured using XRD. The synthesized colloidal MnO_2 particles were supported onto porous aluminum oxide and physically attached to the support free surface via calcinations at 500 °C. MnO_2-coated Al_2O_3 demonstrated an extensive surface area of 140 m^2/g. The catalytic activity of MnO_2-coated AL_2O_3 was evaluated by degrading organic contaminant. Catalytic process in presence of UV-irradiation and H_2O_2 removed 95% of contaminant within 10 min. The mechanism of dye-removal was reported to be a novel combinatorial synergistic effect of adsorption, oxidation, and photocatalysis. Coupling different semiconductor metal oxides together extended sample's light response to visible region and enhance photo-generated e^--h^+ separation efficiency. This study shaded the light on novel high interfacial surface area photocatalyst; that can be easily isolated avoiding contamination with nanoparticles.

Keywords Nanoparticles · Manganese oxide · Adsorption · Photocatalyst · Catalyst support · Water treatment

1 Introduction

The immense demand for drinking water quality and industrial drainage boosts the technologies for adequate and economic water treatment. Combining two or three methods for wastewater treatments into the hybrid process is considered as a new methodology to achieve this purpose [1]. In a hybrid process, different cohesive procedures are combined into one system. Diverse of biological, physical and/or chemical processes could be united, completing each other, forming a hybrid process [2]. Such an approach can rise above any single process disadvantages and can offer synergistic effect with better efficiency and sustainability [3]. Much research work has been directed to the development of hybrid material candidate for adsorption and photocatalysis for water treatment [4]. Photocatalytic degradation of organic compound basically involves three stages:

1. The activation of the photocatalyst by light energy to generate electrons and holes.
2. The holes oxidize water to generate hydroxyl radicals (primary oxidant), and at the same time the electrons reduce oxygen to form other oxidizing agents including more hydroxyl radicals.
3. The radicals oxidize the pollutants eventually to carbon dioxide, water, and simple mineral acids [4–7].

✉ Sherif Elbasuney
s.elbasuney@mtc.edu.eg; sherif_basuney2000@yahoo.com

[1] Head of Nanotechnology Research Centre, Military Technical College, Cairo, Egypt

[2] School of Chemical Engineering, Military Technical College, Cairo, Egypt

TiO_2-coated activated carbon demonstrated several advantages for methyl orange photo-degradation compared to adsorption or photocatalysis [8]. Lim et al. [3] investigated the hybrid process of using adsorption and photocatalysis for organic pollutants degradation using TiO_2/activated carbon (AC). This approach offered many advantages including; TiO_2/AC was reported to be more reliable pollutant removal and more versatile. TiO_2/AC could be more resistant to deactivation. TiO_2/AC provided better mineralization results; the micron size of TiO_2/AC could be easily recovered compared to TiO_2 nanoparticles [3].

The photocatalytic properties of manganese oxide have drawn an increasing attention as its electronic structure is semiconducting [9]. Electronic transitions could occur under irradiation, owing to incompletely occupied d-orbitals. Therefore manganese oxide can act as an effective photocatalyst without doping with other cations [10]. The catalytic action can occur by stimulating the occupied electrons on O-2p to the unoccupied 3d orbits [11, 12]. Manganese oxide was employed to degrade halogenated methane in the gas phase under visible illumination [13–15]. Under UV illumination, manganese oxide demonstrated effective photo-catalytic degradation of methylene blue compared with TiO_2 [9]. This indicates that the photocatalytic activity of manganese oxide could be greater than common catalysts i.e. TiO_2 or ZnO [16]. Manganese oxide can offer significant capabilities including; surface adsorption; oxidation–reduction and photocatalytic-oxidation [17]. These reactions can happen simultaneously and rapidly [18].

Nanosized manganese oxide semiconducter based materials have been found to be good environmental catalysis. To synthesize such material needs knowledge to control its crystal size in the photocatalyst [19]. This is, due to the particles agglomeration in solution which causes the reduction of photocatalytic efficiency. One way to overcome this drawback is to apply solution-based chemical synthetic methodologies such as sol–gel [20], in-situ oxidative method [21] and chemical oxidative polymerization method [22] that can easily disperse the oxide in organic solvent and homogenously load on the supported material. Nanoparticle refers to size of a particle with at least one dimension from 1 to 100 nm [23]. Coupling different semiconductor metal oxides together extend sample's light response to visible region and enhance photo-generated e^--h^+ separation efficiency.

The sustainable fabrication of manganese oxide at the nanoscale is a vital issue for enhanced reactivity [24]. Many researcher investigate the catalytic activity of manganese oxide in different applications [17, 25]. It is broadly established that the classical batch synthesis procedures are laborious and time-consuming. These procedures cannot offer nanoparticles with controlled morphologies. Furthermore, they usually involve nanoparticle drying and sintering processes. Accordingly, these resulted in producing of sturdily bonded or merged particles, with a fundamental reduction in their external surface area and reactivity. There are many techniques for the sustainable fabrication of different nanoparticles however, hydrothermal processing proved to be one of the most promising methods [26–31]. The utilized fluid for hydrothermal processing is supercritical fluid (SCF) [32]. Despite the fact that, supercritical water (ScW) requires severe conditions (Critical temperature and pressure of 374.2 °C and 220.5 bar respectively); it is the common ScF in use for hydrothermal processing [33]. ScW imposes a tremendous number of hydroxide ions (OH^-) and hydrogen ions (H^+). The elevated levels of (OH^-) ions at the critical point can be exploited for nanoparticle fabrication [34, 35]. Nanoparticles can be formulated through, hydrolysis of a metal salt (Eq. 1) that is immediately followed by a dehydration step (Eq. 2) [34, 35].

$$\text{Hydrolysis}: \quad ML_x + xOH^- \rightarrow M(OH)_x + xL^- \tag{1}$$

$$\text{Dehydration}: \quad M(OH)_x \rightarrow MO_{x/2} + \frac{x}{2} H_2O \tag{2}$$

Hydrothermal fabrication includes instantaneous mixing of metals salts with ScW. Consequently, nanoparticles are formed at the edge of the two liquids [22, 23]. While most researches on manganese oxide photocatalysis have been directed to the gaseous degradation of organic compounds, rare research has been directed on adsorption, oxidation and photocatalytic activity of manganese oxide nanoparticles in solution.

This work demonstrates a new procedure for manufacturing MnO_2 nanoparticles of 20 nm average particle size by sustainable hydrothermal technique. The developed colloidal particles were supported on a porous aluminium catalyst support of 185 m^2/g and physically attached to the support surface via calcinations at 500 °C. MnO_2-supported on Al_2O_3 demonstrated a surface area of 140 m^2/g. This approach offered superior photocatalytic performance; the proposed mechanism for organic dye-removal is a combination effect of adsorption, oxidation, and photocatalysis. Under optimized photocatalytic process with UV-irradiation and H_2O_2 concentration, MnO_2 demonstrated 95% removal of MB within 10 min. In the meantime, the catalyst can be easily isolated avoiding contamination with nanoparticles.

2 Experimental Work

2.1 Hydrothermal Fabrication of MnO_2 Nanoparticles

Hydrothermal processing method was used to manufacture manganese oxide nanoparticles where, the manganese metal salt flow (B) was immediately mixed with the flow (A) of

supercritical water (ScW). Nanoparticles were continuously produced in the reactor (R) at the boundary of the two fluids. Flow (A) was 20 ml/min ScW at a temperature of 400 °C and a pressure of 240 bar. 0.05 M manganese acetate was manipulated as the metal salt precursor, flow (B), with the flow rate (10 ml/min). The complete manufacture procedure and more details about the hydrothermal processing of various forms of manganese-oxides can be found in the following reference [36, 37].

2.2 MnO_2 Nanoparticles Characterization

Transmission Electron Microscope (TEM) (JEM-HR-2100, Joel Corporation) and Scan Electron Microscope (SEM) (Zeiss EVO-10, Carl Zeiss Corporation) were used to study the morphological structure of manufactured MnO_2 nanoparticles. The crystalline phase of manganese oxide was examined using XRD D8 advance by Burker Corporation.

2.3 Supporting MnO_2 Nanoparticles on a Porous Aluminum Substrate

Colloidal MnO_2 nanoparticles were flocculated from their synthesis medium, excess water was decanted. Colloidal MnO_2 particles were integrated onto the porous structure of aluminum substrate by sonication for 2 h. The porous substrate was separated and calcinated at 500 °C for 2 h. This approach could secure high crystalline structure and effective physical attachment to the substrate surface. Figure 1 shows the change of color of the substrate from white yellow to dark brown after calcination.

Figure 1 demonstrated that a uniform and effective coating with MnO_2 nanoparticles was achieved. MnO_2 loading level was found to be 17 wt%.

2.4 Surface Area and Porosity Measurements

The porosity of developed photocatalyst was examined using the nitrogen adsorption–desorption method in a Micromeritics apparatus. The relative pressure (p/p_0) of the isotherms was measured for a relative range between 0.01 and 0.99. For every pressure step, and after equilibrium had been verified the amount of N_2 adsorbed was measured. The photocatalyst porosity parameters such as surface area, pore volume, pore diameter, and micropore surface area were then calculated. The Brunauer-Emmett-Teller (BET) investigation was accomplished at a relative pressure (p/p_0) between 0.06 and 0.2 [38]. While N_2 adsorbed at a relative pressure of 0.975 was employed for the calculation of the total pore volume. Horvath-Kawazoe and BJH models were used in the estimation of the size distribution of micropores and mesopores, respectively. The micropore volume was measured at (p/p_0) of 0.2. However, the mesopore volume was estimated by subtracting the amount of N_2 adsorbed at (p/p_0) of 0.2 from that adsorbed at (p/p_0) of 0.99 [38].

2.5 Adsorption Measurements

The kinetic adsorption measurements were conducted using batch equilibrium techniques in Erlenmeyer flasks at 25 °C. 0.5 g of catalyst was added to 50 ml of MB aqueous solution with a concentration range of 10–30 mg/l under a stirring rate of 100 rpm and natural pH (pH 6.2). Time recording started with the addition of the catalyst. At each time interval, 2 ml

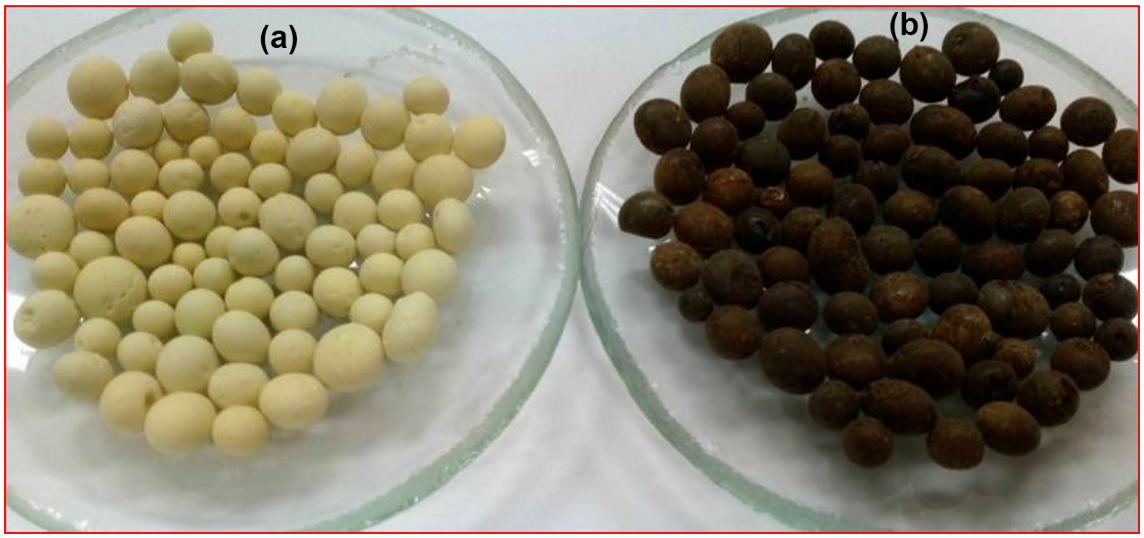

Fig. 1 Photo images of an aluminum substrate (**a**), and MnO_2-coated aluminum substrate (**b**)

were taken from the solution to be analyzed in a UV–Vis spectrophotometer (Shimadzu UV-1700 UV–Vis) at 664 nm for MB. The adsorption capacity at time t, Q_t (mg/g) was determined using Eq. 3.

$$Q_t = \frac{V(C_0 - C_t)}{m} \tag{3}$$

where C_0 is the initial concentration of the dye, C_t is the concentration of the dye at measuring time *t, m* is the mass of the MnO_2-coated aluminum catalyst, and V is the volume of the MB aqueous solution.

For the adsorption experiments, a fixed sample weight of 500 mg was added at different initial concentrations (10–30 mg/l) of MB. After every 10 min. the concentration was measured with a UV–Vis. The adsorption capacity of the prepared MnO_2 particles, Q_e (mg/g), was measured at equilibrium and given by Eq. 4.

$$Q_e = \frac{V(C_0 - C_e)}{m} \tag{4}$$

where C_e is the concentration of the liquid at equilibrium. The experiments were accomplished at a natural pH of 6.2 and the efficiency of the removal of methylene blue was described as Eq. 5.

$$Removal(\%) = \frac{(C_0 - C_e) \times 100}{C_0} \tag{5}$$

2.6 Photochemical Measurements

Photochemical measurements were conducted in a 250-ml glass immersed in a photochemical reactor, charged with 50 ml of MB aqueous solution, where the solution is illuminated using a low-pressure 10 Watts mercury lamp with an emittance of 90% at 254 nm, placed axially and retained in a quartz immersion tube. Samples (ca. 2 ml) were taken at regular intervals for UV–Vis measurements at the maximum absorption peak of methylene blue ($\lambda_{max} = 664$ nm). To guarantees that the adsorption–desorption equilibrium was established, the solution was stirred under dark conditions for 120 min.

3 Results and Discussions

3.1 Characterization of Synthesized MnO_2

TEM micrographs demonstrated colloidal mono-dispersed MnO_2 of an average particle size of 20 nm (Fig. 2a). While (Fig. 2b) verified the lattice high crystalline structure.

Figure 2 demonstrated MnO_2 nanoparticles, with consistent product quality, have been developed using hydrothermal processing. It is established that similar particles are expected to be developed as nucleation and subsequent particle growth are the same for all particles [26, 39]. Manganese (IV) oxide crystalline structure was reported from XRD diffractogram (Fig. 3).

The spectrum above shows nine sharp peaks which agreed with the literature and Joint Committee on Powder Diffraction Standards (JCPDS) [10, 40]. Figure 4 shows that the

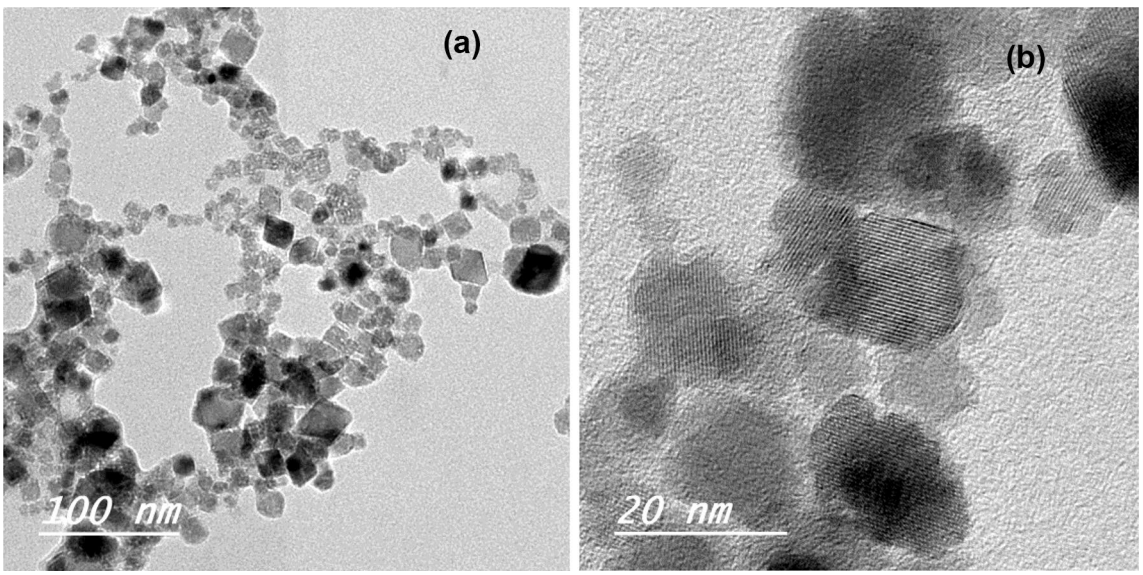

Fig. 2 TEM micrographs of MnO_2 nanoparticles: morphology (**a**), lattice from **b**

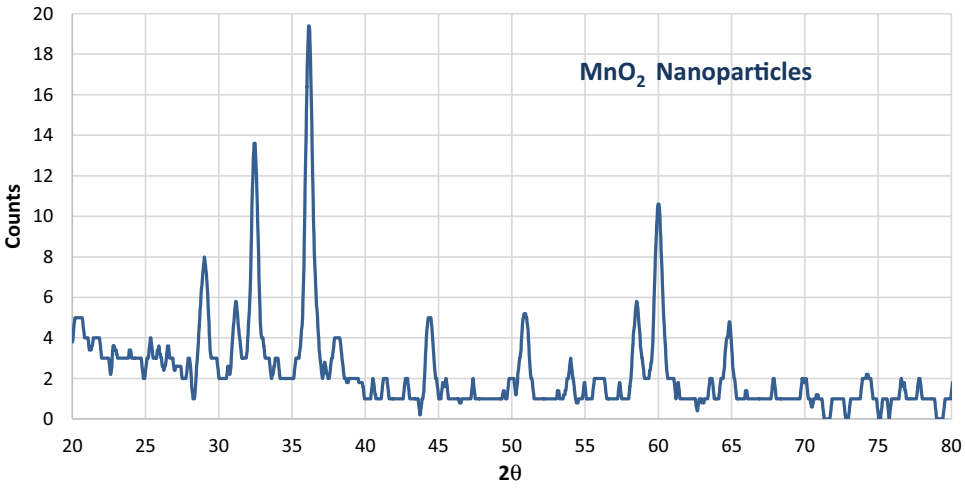

Fig. 3 XRD spectrum of prepared MnO_2 nanoparticles

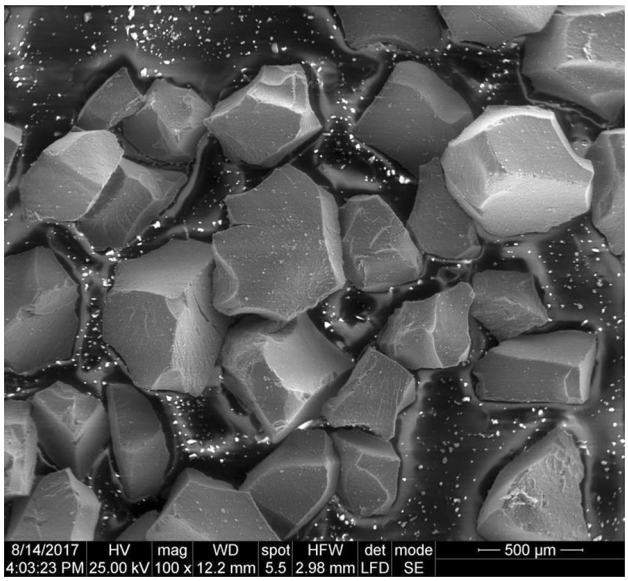

Fig. 4 SEM micrographs of developed MnO_2 nanoparticles

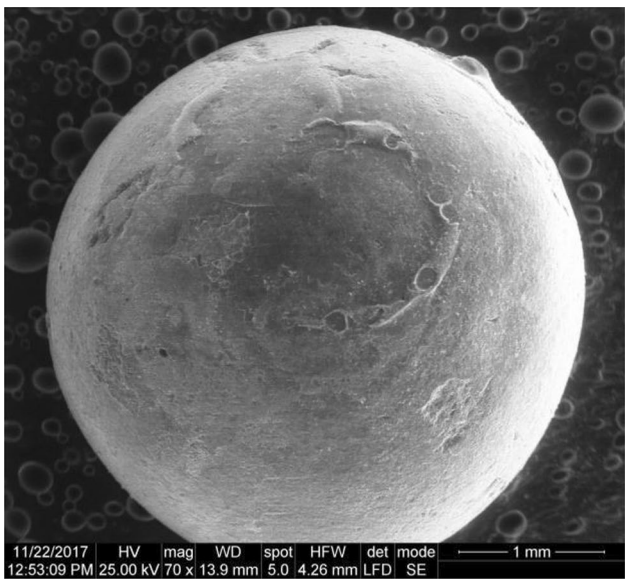

Fig. 5 MnO_2 supported on Al_2O_3 porous substrate micrographs by SEM

morphology of MnO_2 particles visualized by SEM which demonstrated a great tendency of the particles to aggregate under the drying process.

It has been recognized that nanoparticles have a great tendency to aggregate over the drying process with a radical lessening in their reactivity and surface area [26]. This is why colloidal MnO_2 nanoparticles were integrated into/onto the catalyst support in an attempt to maintain their high interfacial surface area and reactivity [11, 41].

3.2 Characterization of MnO_2-Supported on a Porous Substrate

SEM micrograph of MnO_2-coated Al_2O_3 demonstrated uniform coating throughout the porous substrate surface (Fig. 5).

Figure 5 reveals sphere porous substrate of 4 mm diameter that is uniformly coated with MnO_2 nanoparticles; there were no aggregates over the surface. The amount of N_2 adsorbed at 77 k was plotted against the relative pressure shown in Figs. 6 and 7 for Al_2O_3 substrate and MnO_2-coated Al_2O_3, respectively. The isotherm is consolidation of types I and IV isotherms which are characteristic for micro-mesoporous adsorbent. The type IV isotherm

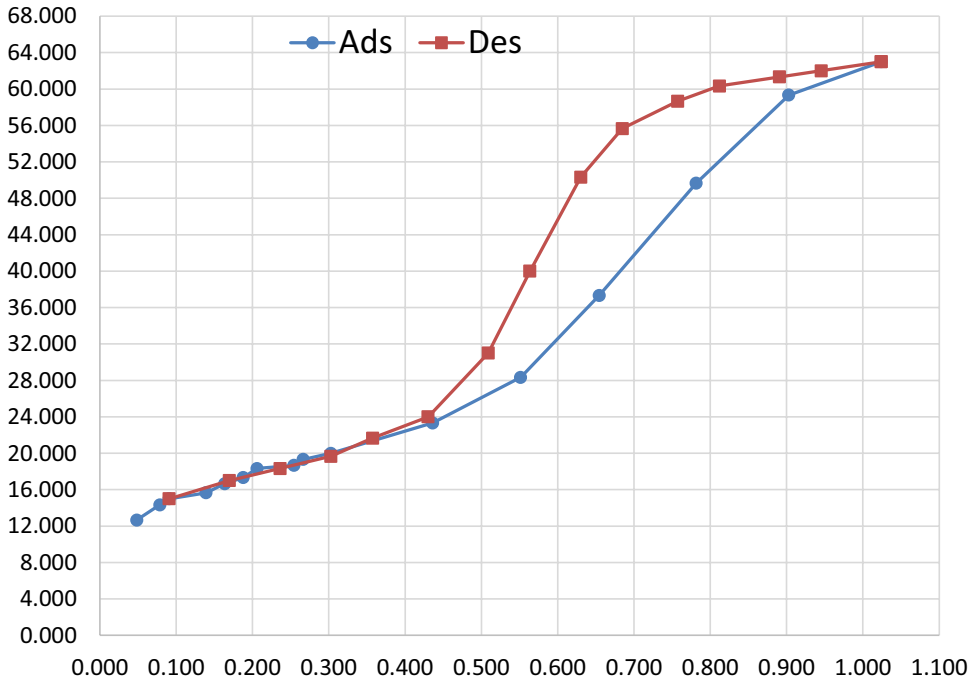

Fig. 6 Adsorption profiles of N_2 at 77 K on the alumina porous substrate

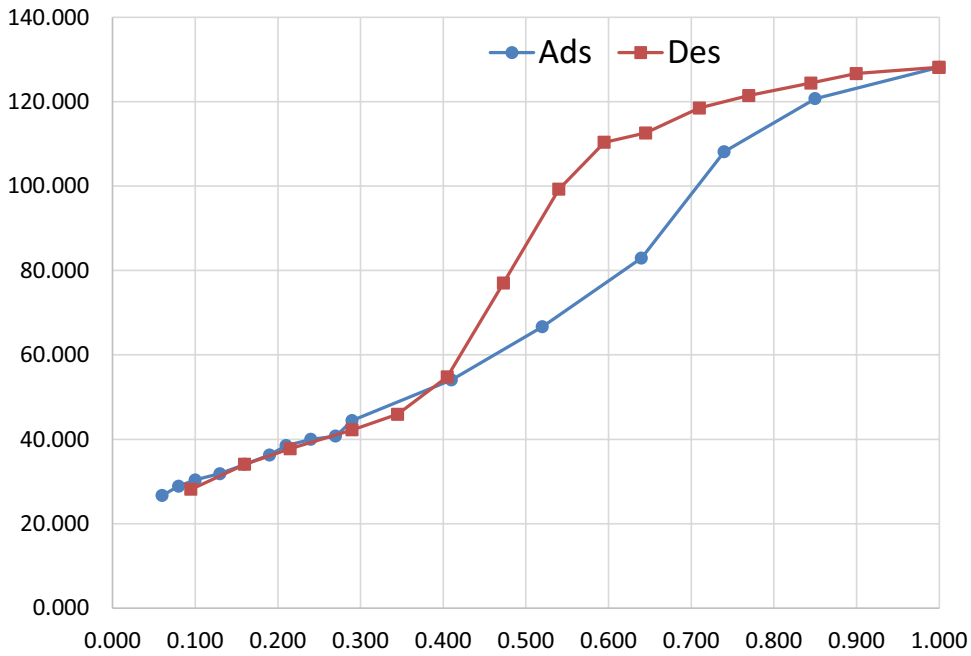

Fig. 7 Adsorption profiles of N_2 at 77 K on the MnO_2-coated Al_2O_3

arises from both mesoporous and non-porous adsorbent, where the comprehensive filling of the smallest capillaries has arisen, it also defines a multilayer adsorption process. While type I isotherm arises from monolayer adsorption which is distinctive for microporous adsorbent. In these micropores, filling takes place significantly at a relatively low partial pressure less than 0.1 p/p_0, the adsorption process is complete at a partial pressure around 0.9. Moreover, nitrogen uptake takes place mostly at a partial pressure of more than 0.4. This indicates that the meso- or macro-pore structure in the sample was significantly developed. Both isotherms are distinguished by hysteresis loops, which developed in the multilayer domain of physisorption isotherms. Generally, these types of loops are accompanying with capillary condensation which is distinctive and reproducible for most mesoporous adsorbents.

BJH adsorption pore distribution of mesopores size for MnO_2-coated Al_2O_3 is represented in Fig. 8, where broad peaks in the meso- and macropore range were observed. The main characteristic pore properties of the Al_2O_3 and MnO_2-coated Al_2O_3 are listed in Table 1.

The results of Table 1 revealed that the synthesis procedure does not affect the surface area of the catalyst and both Al_2O_3 and MnO_2-coated Al_2O_3 have high pore volumes and surface areas in comparison with other adsorbents and photocatalysts found in the literature [42–44]. The percent

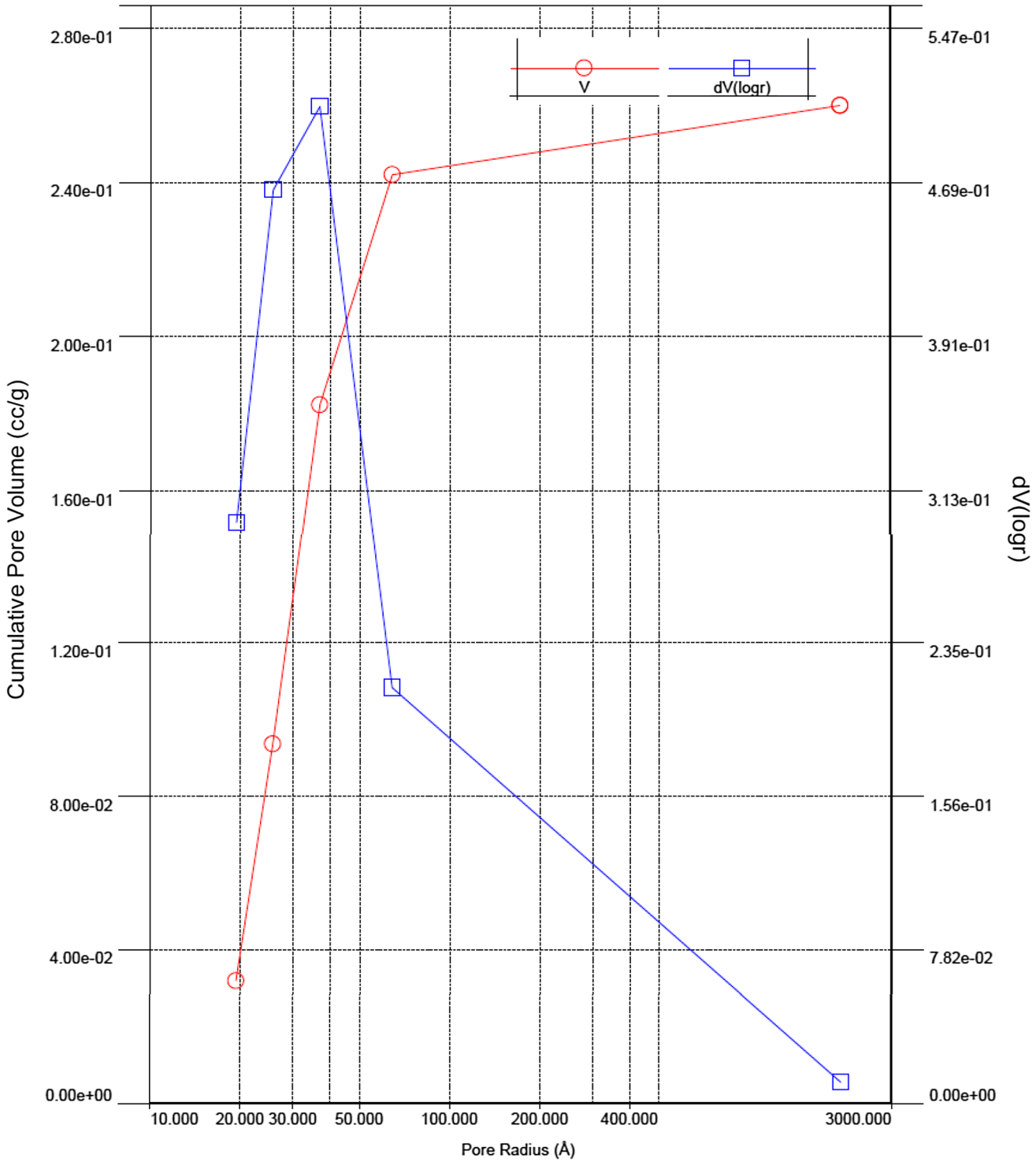

Fig. 8 The BJH adsorption pore distribution of meso-size for the MnO_2-coated Al_2O_3

Table 1 The characteristic pore properties of Al_2O_3 and MnO_2-coated Al_2O_3

Nomenclature	S_{BET}[a] ± 10 (m^2/g)	V_t[b] ± 0.01 (cm^3/g)	V_{mic}[c] ± 0.01 (cm^3/g)	V_{mes}[d] ± 0.01 (cm^3/g)	D_p[e] ± 0.01 (nm)
Al_2O_3	185	0.315	0.170	0.145	1.91
MnO_2-coated Al_2O_3	140	0.210	0.121	0.089	2.10

[a]BET surface area

[b]Total pore volume

[c]Micropore volume estimated by the Horvath-Kawazoe model from the amount of N_2 adsorbed at a relative pressure p/p_0, of 0.20

[d]Mesopore volume, estimated by deducting the amount of N_2 adsorbed at p/p_0 of 0.2 from that adsorbed at p/p_0 of 0.99

[e]Mean pore diameter is estimated from ($4\ V_t/S_{BET}$)

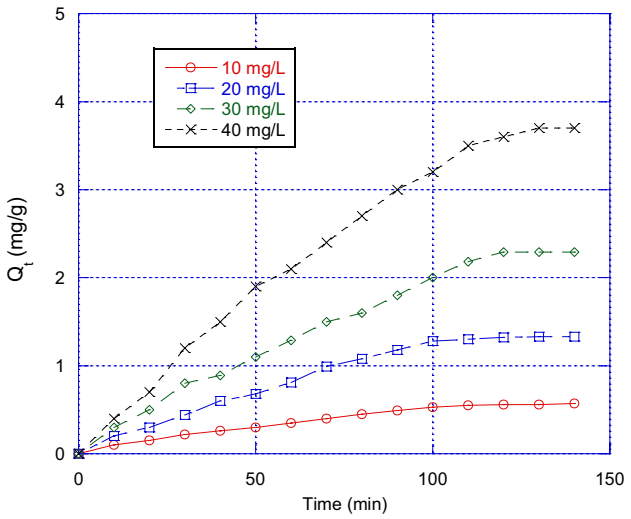

Fig. 9 Adsorption kinetic of a MnO_2-coated Al_2O_3 catalyst, experimental conditions: pH 6.2, m (catalysts) = 0.5 g, V (solution) = 50 ml, r (rate) = 100 rpm, T = 25 °C

of micro-pore volume (0.121 cm^3/g) to the total pore volume (0.210 cm^3/g) of the MnO_2-coated Al_2O_3 catalyst is approximately 60%. Therefore, it is a good candidate as adsorbent and photocatalyst.

3.3 Adsorption of Methylene Blue on MnO_2-Coated Al_2O_3

The adsorption of MB on the MnO_2-coated Al_2O_3 catalyst at several initial dye concentrations in the range from 10 to 30 mg/l, while maintaining other experimental parameters to be constant are shown in Fig. 9.

Figure 9 revealed that the adsorption of MB on the MnO_2-coated Al_2O_3 catalyst can be divided into two time period steps. The first step, there was an increase in the adsorption capacity in a first step reaching a plateau in the second step, which corresponds to the maximum amount that could be adsorbed after around 120 min. As predictable, as the initial concentration increases the adsorbed amount increase due to an increase of the driving forces. To gain a better understanding of the adsorption mechanism, the adsorption isotherms were studied. The isotherms were recorded at a temperature of 25 °C and displayed for the adsorption of MB onto MnO_2-coated Al_2O_3 catalyst.

In an attempt to identify the interactions between MnO_2-coated Al_2O_3 catalyst and MB, the experimental data points were estimated and fitted using the Langmuir, Freundlich and Sips modeling [45, 46]. The empirical models used in this study involve two-parameter as well as three-parameter equations, at a constant temperature, describing the nonlinear equilibrium between the pollutant in solution (C_e) and the adsorbed amount (Q_e) [47–49]. The hypothesis of the Langmuir isotherm model is based on a homogeneous energy of adsorption at the adsorbent surface in the presence of a monolayer coverage by the dye at all surfaces of the adsorbent, and in this case, all sorption sites are equal [50, 51]. Equation (6) describes the Langmuir equation, while Eq. (7) shows the linearized form of it.

$$q = \frac{q_m\, b\, C_e}{1 + b\, C_e} \tag{6}$$

$$\frac{C_e}{q} = \frac{1}{q_{m\,b}} + \frac{C_e}{q_m} \tag{7}$$

where b is the Langmuir constant, q_m is the adsorption amount (mg/g) of the solid at monolayer inclusion. b and q_m can be derived from the linear plot of C_e/q versus C_e. Table 2 shows the calculated values of b and q_m along with the correlation coefficients. The dimensionless constant (R_L) that is the fundamental characteristic of the Langmuir isotherm is given by:

$$R_L = \frac{1}{(1 + K_L C_i)} \tag{8}$$

where C_i (mg/L) is the highest initial concentration of MB and (R_L) values between 0 and 1 indicate favourability of adsorption. (R_L) was calculated to be 0.45 in the current study which implies favorable adsorption of MB onto MnO_2-coated Al_2O_3 catalyst surface. Figure 10 demonstrates the Langmuir adsorption isotherm and experimental data of MB adsorption over the MnO_2-coated Al_2O_3 catalyst.

The hypothesis of the Freundlich isotherm model is not based on limited levels of sorption homogeneous or location energies, instead, the model describes the exponential distribution of active centers and heterogeneous surfaces [24]:

$$q = k\, C_e^{1/n} \tag{9}$$

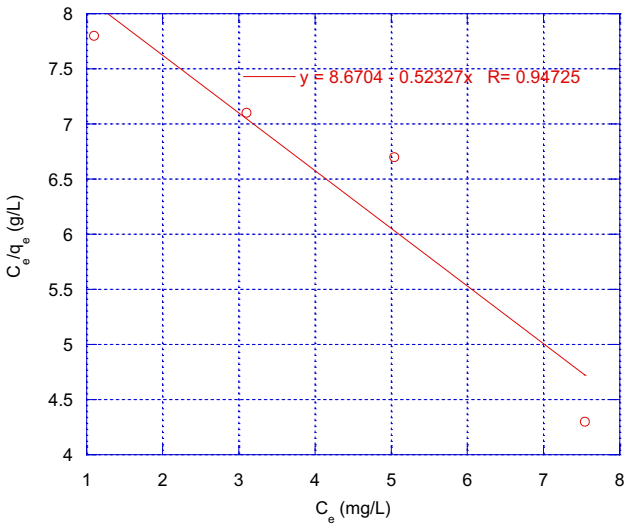

Fig. 10 Langmuir adsorption isotherm along with MB adsorption experimental data using a MnO_2-coated Al_2O_3 catalyst

n and k are the constants of adsorption potential and adsorption depth respectively. Equation (9) can be linearized as shown in the equation below:

$$\ln q = \ln k + \frac{1}{n} \ln C_e \tag{10}$$

The value of n and k can be calculated from the slope and intercept of the linear plot of ln q against ln C_e. The Freundlich isotherm implements no data on the monolayer adsorption density in contrast with the Langmuir model. Figure 11 shows the Freundlich adsorption isotherm and experimental data of MB adsorption over the MnO_2-coated Al_2O_3 catalyst. Table 2 shows the values of

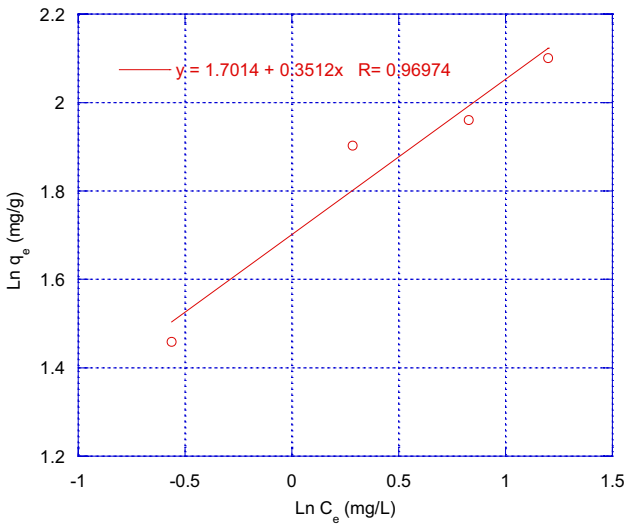

Fig. 11 Freundlich adsorption isotherm and experimental data of MB adsorption over the MnO_2-coated Al_2O_3 catalyst

n and k obtained from the linear plots and the regression correlation coefficients.

The three-parameters Sips isotherm equation is postulated from the restriction behavior of the Langmuir and Freundlich isotherms. The model is adequate for confined adsorption without adsorbate intraparticle interactions [15]. In the circumstance of a low value of C_e, Sips isotherm efficiently lessens to Freundlich, while at a high value of C_e, it can be used to predicts the monolayer sorption characteristic of Langmuir. The linearized form of Sips isotherm equation is expressed as:

$$\frac{1}{q_e} = \frac{1}{Q_{\max} k_s} \left(\frac{1}{C_e}\right)^{1/n} + \frac{1}{Q_{\max}}, \tag{11}$$

where K_S in L/mg is the Sips equilibrium constant and Q_{max} in *mg/g* is the maximum adsorption amount values obtained from the slope and intercept of the linear plot, respectively as shown in Fig. 4. Whereas n is a dimensionless factor of heterogeneity, its value is between 0 and 1. This factor can also be utilized to define the adsorption heterogeneity. When $n = 1$, the Sips equation lessens to the Langmuir equation and it specifies a homogeneous adsorption [52, 53]. Figure 12 shows the Sips adsorption isotherm and experimental data of MB adsorption over the MnO_2-coated Al_2O_3 catalyst. Table 2 shows the isotherm models parameters and correlation coefficient (R^2) of MB adsorption over MnO_2-coated. The R^2 coefficient was derived to help in indicating the most precise model in describing the obtained experimental results.

The highest values of R^2 Correlation coefficient, $R^2 = 0.99$, obtained from applying Sips modeling suggested that the results obeyed this isotherm, then followed by the Freundlich modeling isotherm, $R^2 = 0.96$, and the Langmuir model, $R^2 = 0.95$. Moreover, it should be recognized that both Langmuir and Freundlich models have only two adaptable parameters while the Sips model has three. As far as we know, in general, the accuracy and flexibility of the model increase with increasing adjustable parameters.

Table 2 Isotherm models parameters and correlation coefficient (R^2) of MB adsorption over the MnO_2-coated Al_2O_3 catalyst

Isotherm	Parameters	R^2
Langmuir	$K_L = 25.489$ L/mg $Q_m = 0.037$ mg/g	0.95
Freundlich	$K_F = 0.325$ (L/g) $1/n = 0.69$	0.96
Sips	$K_S = 6.27 \times 108$ L/mg $Q_{max} = 0.013$ mg/g $n = 0.24$	0.99

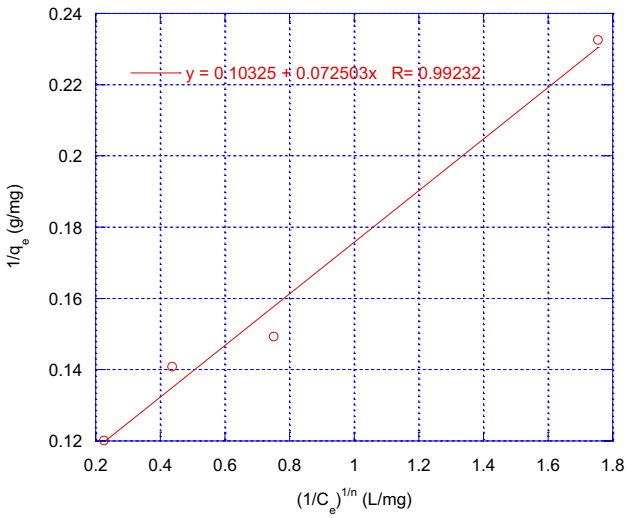

Fig. 12 Sips adsorption isotherm and experimental data of MB adsorption over the MnO_2-coated Al_2O_3 catalyst

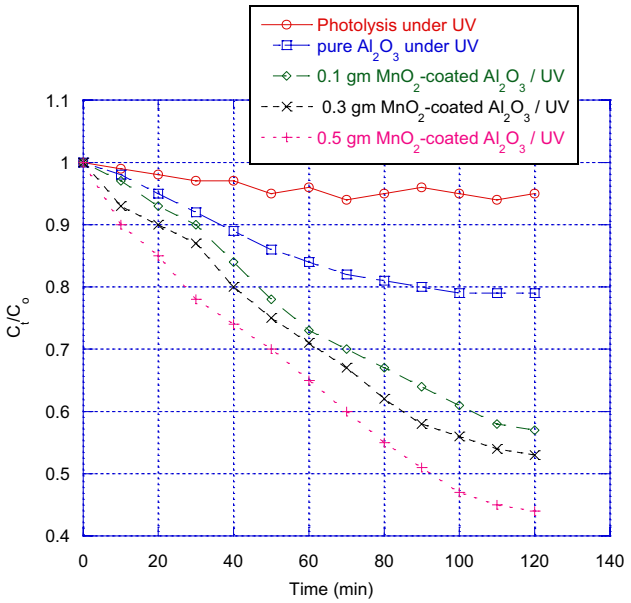

Fig. 13 Kinetic of photocatalytic MB degradation over the different dose of MnO_2-coated AL_2O_3. Experimental conditions: pH 6.2, V(solution) = 50 ml, C_0 = 20 mg/l, T = 25 °C

3.4 Photocatalytic Degradation Measurements

This experimental section was conducted to verify that the adsorption–desorption equilibrium was established, the solution was stirred under dark conditions for 120 min. Figure 13 shows the photodegradation of methylene blue (MB) over different dose of MnO_2-coated AL_2O_3 under UV illumination compared to methylene blue photolysis under the Ultra Violet light only, in the absence of catalysts in the solution. To ensure that an equilibrium is reached in the establishment of adsorption–desorption (not shown) and prior to the photocatalytic experiment, the concentration of MB was monitored after 120 min. of magnetically stirring in darkness. The results showed that a faster degradation of MB solution was observed after exposing to 120 min. of UV radiation when MnO_2-coated AL_2O_3 were used as photocatalyst.

Under UV illumination, MnO_2-coated AL_2O_3 particles interacted with Ultra Violet light to generate hole (h^+) and electron (e^-). The holes were trapped by O_2 or H_2O at the surface of the catalyst particle yielding $H\dot{O}$ radicals and H^+, which effectively destroyed MB by acting as an oxidation agent. These agents could be used to mineralize organic pollutants to smaller and less hazardous species, eventually generating CO_2, H_2O, and other degradation through other processes [54, 55]. Reactions in the equations from (12) to (21), described the simplified mechanism of MnO_2 activation with UV light [17, 56, 57].

Furthermore, during the photosensitized oxidation process in the presence of catalysts (reaction 16), methylene blue dye becomes excited by injecting an electron into the conduction band. The dye was then changed to a cationic dye radical that was subjected to degradation, yielding products in conformity with the following reactions (17) to (21) [22].

$$MnO_2 + h\upsilon \rightarrow MnO_2\left(e^-_{CB} + h^+_{VB}\right) \quad (12)$$

$$MnO_2\left(h^+_{VB}\right) + H_2O \rightarrow MnO_2 + H^+ + OH^{\cdot} \quad (13)$$

$$MnO_2\left(e^-_{CB}\right) + O_2 \rightarrow MnO_2 + O_2^{\cdot -} \quad (14)$$

$$O_2^{\cdot -} + H^+ \rightarrow HO_2^{\cdot} \quad (15)$$

$$MB^* + MnO_2 \rightarrow MB^{\cdot +} + e^-_{CB}\left(MnO_2\right) \quad (16)$$

$$O_2 + e^- \rightarrow O_2^{\cdot -} \quad (17)$$

$$MB^{\cdot +} + OH^- \rightarrow MB + OH^{\cdot} \quad (18)$$

$$MB^{\cdot +} + OH^{\cdot} \rightarrow H_2O + CO_2 + \textit{Degredation products} \quad (19)$$

$$MB^{\cdot +} + O_2^{\cdot -} \rightarrow \textit{Degredation products} \quad (20)$$

$$MB^{\cdot +} + HO_2^{\cdot} \rightarrow \textit{Degredation products} \quad (21)$$

In addition, $H\dot{O}$ attacked the MB molecule through a hydrogen extraction effect or hydroxyl addition, where MB was converted to H_2O and CO_2 through various paths reactions [58, 59].

Normally, the electronic configuration of the catalyst played a great role in its photocatalytic activity [60, 61]. In Manganese oxide, the d–d electronic transitions commonly arise under irradiation because of unoccupied d-orbital. Consequently, to a degree manganese oxide can be successfully utilized as a photocatalyst without doping other cations [62]. The photochemical reaction usually happened as a result of excitation of the O-2p occupied electrons of manganese

oxide to the unoccupied orbits (mainly Mn-3d) when the light energy was larger than the energy of the orbit gap [10, 63]. It is verified by the case that the photo-induced electric current of manganese oxide was noticed [41]. Moreover, the physiochemical, surface area, severe defects and non-stoichiometry properties of MnO_2 leads to its application as an adsorbent, oxidant and catalysis in many studies [1, 64, 65]. A first-order model was used to express the kinetics of the degradation of different photocatalysts shown in the equation [3]:

$$\ln \frac{C}{C_0} = k_{app}\, t \tag{22}$$

where k_{app} is the first-order reaction apparent rate constant (min^{-1}), C_0 is the equilibrium concentration of the dye solution after adsorption in dark conditions and C is the residual concentration at a given time. Figure 14 shows a plot of ln (C_0/C) against t. The results showed that the photocatalytic activity for MB photodegradation over MnO_2-coated AL_2O_3 particles, determined from the k_{app}, was increased with increasing the amount of catalyst. Where, the kinetic constants, k_{app} (min^{-1}), were 51×10^{-4} min^{-1}, 56×10^{-4} min^{-1}, and 69×10^{-4} min^{-1} for 0.1, 0.3 and 0.5 g of catalyst, respectively. Applying the best photocatalyst dosage decreases the energy and cost while maximizing photocatalytic accomplishments [8]. However, some researcher reported an increase of the number of photons absorbed on the photocatalyst by increases the dosage of the photocatalyst. Consequently, these motivate the increases in the creation of hydroxyl radicals and electron–hole pairs, which leads to higher removal efficiency.

Usually, the adsorption of organic pollutants on photocatalyst is vital for the heterogeneous photocatalytic reactions [2]. Coupling photocatalysis and adsorption simultaneously could enhance the rate of degradation of the catalysts towards organic pollutant [66]. Consequently, the removal of organic contaminants rises significantly with the increase of the amount adsorbed of the contaminants on the catalyst's surface in a certain range.

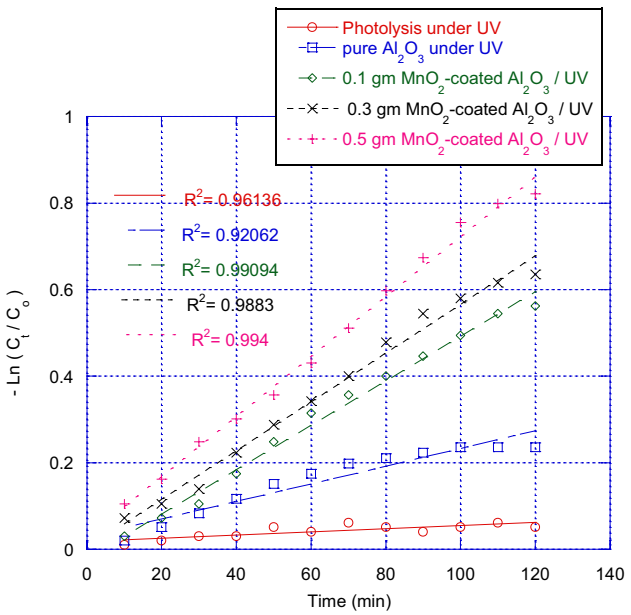

Fig. 14 Kinetics plots for linear fitting of data obtained from pseudo-first-order reaction model for MB degradation under UV light irradiation and different dose of MnO_2-coated Al_2O_3 particles. Experimental conditions: pH 6.2, V(solution) = 50 ml, C_0 = 20 mg/l, T = 25 °C

3.5 Effect of Oxidant

UV-irradiation generates hydroxyl radicals in water by UV-irradiation which can form H_2O_2. To investigate whether additional H_2O_2 has an influence on the overall degradation of MB, a few experiments were conducted at different concentrations of added hydrogen peroxide. So, photodegradation experiments were repeated with MB solutions with a hydrogen peroxide with concentration of 0.15 mM, 0.3 mM and 0.6 mM. This will help study the effect of adding hydrogen peroxide on the degradation of MB at pH 6.2, V (solution) = 50 ml, C_0 = 20 mg/l, T = 25 °C. The concentration of the dye was monitored after the establishment of adsorption–desorption equilibrium by magnetically stirring in the dark for 120 min before the photocatalytic experiment.

Figure 15 shows the effect of the addition of different amounts of hydrogen peroxide on the MB solution. It is clear from the figure below that the addition of hydrogen peroxide had a positive influence on the degradation of MB in comparison with its absence. The larger the amount of hydrogen peroxide in presence of UV-irradiation increases the degradation of MB and could remove up to 95% of MB within 10 min. While the percent removal of MB by adsorption and UV-irradiation alone reached 35% and 56% within 120 min. respectively, as demonstrated in Fig. 16.

Under UV-irradiation, H_2O_2 decomposes readily into $\dot{O}H$ which leads to high degradation rate, according to the following equations.

$$H_2O_2 + UV \rightarrow 2\dot{O}H \tag{23}$$

$$\dot{H} + H_2O_2 \rightarrow \dot{O}H + H_2O \tag{24}$$

UV-irradiation alone produces a small amount of hydrogen peroxide which will not be sufficient to dissociate a large number of hydroxyl radicals. Therefore, an additional amount of hydrogen peroxide is added to accelerate the degradation process significantly. Hydroxyl radicals formation will be increased by hydrogen peroxide in two ways. The first way is by the self-decomposition due to the UV-irritation or as shown in reactions (23) and (24) where hydrogen

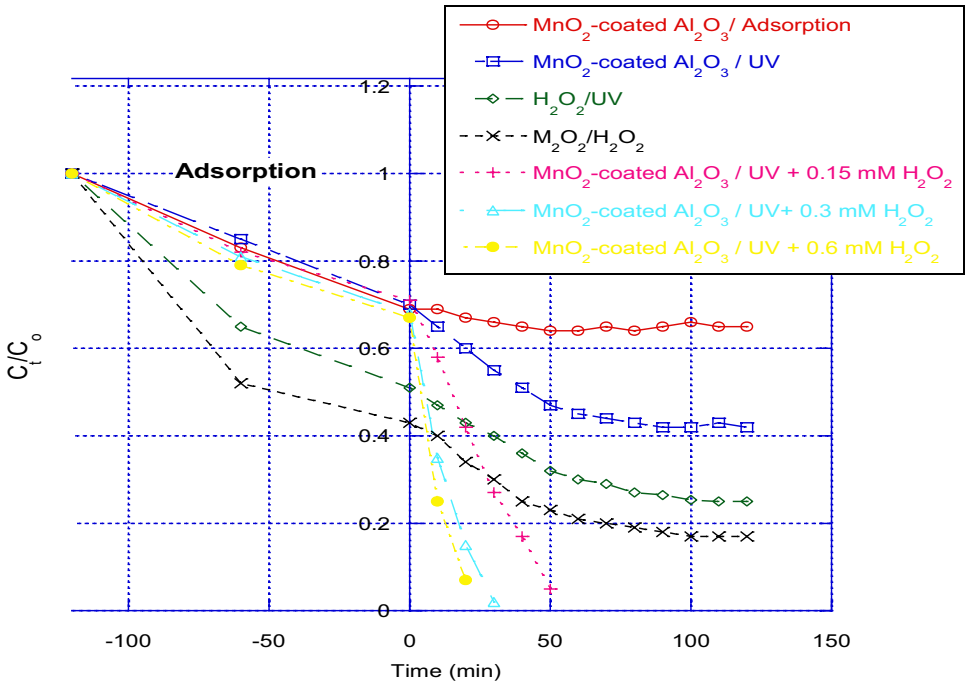

Fig. 15 Effect of H_2O_2 addition on the degradation of MB compared with the results obtained due to adsorption, H_2O_2/UV, M_2O_2/H_2O_2 and photocatalytic, at pH 6.2, V(solution) = 50 ml, C_0 = 20 mg/l, T = 25 °C

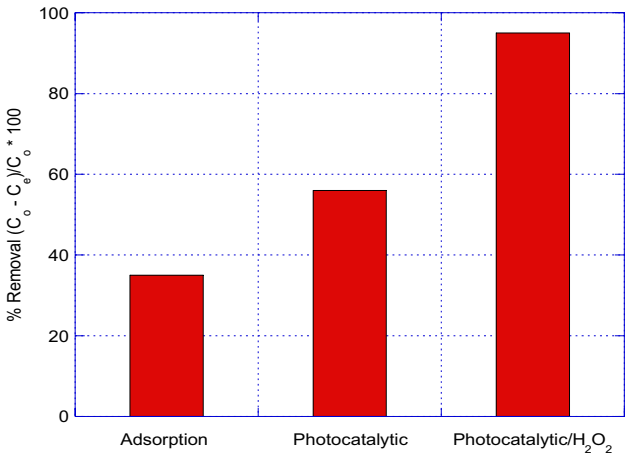

Fig. 16 Comparison between the percent removal of MB by adsorption, photocatalytic and photocatalytic in presence of H_2O_2 (0.6 M) after 10 min, pH 6.2, V(solution) = 50 ml, C_0 = 20 mg/l, T = 25 °C

peroxide reduction occurs at the conduction band of the photocatalyst. It can be established that the acceleration of photocatalytic degradation of organic compounds can be increased significantly by the addition of external oxidants that increase the decomposition rate such as hydrogen peroxide. Hydrogen peroxide undergoes photolysis readily decomposing into hydroxyl radicals as the dissociation energy of O–H bond in the water molecule is 418 kJ/mol which is almost double the dissociation energy that of the O–O bond in the hydrogen peroxide molecule which is 213 kJ/mol. Nevertheless, many research papers that reported the addition of hydrogen peroxide to improve the rate of degradation of organic compounds, it is clear that the optimum amount of hydrogen peroxide added highly depends on the configuration of the equipment, the type of organic compounds and the operating conditions used. Consequently, all of these parameters have great influence on the creation of hydroxyl radicals in the reaction medium. As a final point, the concentration of hydrogen peroxide used should not be more than the optimum value as that it can recombine with the ȮH and result in a decrease in the efficiency of degradation.

4 Conclusion

In this work, MnO_2 nanoparticles of 20 nm average particle size were synthesized successively using hydrothermal synthesis approach. The synthesized colloidal MnO_2 nanoparticles were physically attached to the free surface of the porous support (Al_2O_3) via calcinations. This approach leads the colloidal MnO_2 nanoparticles to be integrated into/onto the catalyst support without aggregation, to maintain their high surface area. The adsorption and photocatalytic degradation activity of MnO_2-coated AL_2O_3 were investigated by degrading organic contaminant (MB) at ambient conditions. The developed catalyst offered superior photocatalytic performance and displayed rapid deterioration of methylene blue (MB) under optimum conditions. And more easily recovered than the MnO_2 nanoparticles. Adsorption results showed that isotherms followed the Sips Model as it had the highest R^2 value of 0.99. While the nitrogen adsorption–desorption isotherm revealed that the prepared catalyst is micro-mesoporous solid with a high surface area of

140 m^2/g. Generally, this approach can rise above any separated process disadvantages where; (1) The porous support can offer extensive surface area and reactivity. (2) Any toxic intermediates can be adsorbed and oxidized; thus, secondary pollution can be prevented. (3) The high removal efficiency of the hybrid photocatalysts is maintained for a long time. (4) The photocatalyst can be easily isolated avoiding contamination with nanoparticles.

References

1. H. Atout et al., Integration of adsorption and photocatalytic degradation of methylene blue using\hbox TiO_2 supported on granular activated carbon. Arab. J. Sci. Eng. **42**(4), 1475–1486 (2017)
2. S. Liu et al., Synthesis and adsorption/photocatalysis performance of pyrite FeS_2. Appl. Surf. Sci. **268**, 213–217 (2013)
3. T.-T. Lim et al., TiO_2/AC composites for synergistic adsorption-photocatalysis processes: present challenges and further developments for water treatment and reclamation. Crit. Rev. Environ. Sci. Technol. **41**(13), 1173–1230 (2011)
4. Y. Wang et al., Visible light driven type II heterostructures and their enhanced photocatalysis properties: a review. Nanoscale **5**(18), 8326–8339 (2013)
5. A. Šutka et al., Photocatalytic activity of anatase–nickel ferrite heterostructures. physica status solidi (a). **212**(4), 796–803 (2015)
6. R. Solomon et al., Enhanced photocatalytic degradation of azo dyes using nano Fe_3O_4. J. Iran. Chem. Soc. **9**(2), 101–109 (2012)
7. A. Gutierrez-Mata et al., Recent overview of solar photocatalysis and solar photo-fenton processes for wastewater treatment. Int. J. Photoenergy (2017) https://doi.org/10.1155/2017/8528063
8. Y. Li et al., Photocatalytic degradation of methyl orange by TiO_2-coated activated carbon and kinetic study. Water Res **40**(6), 1119–1126 (2006)
9. L. Zhang, D. He, P. Jiang, MnO_2-doped anatase TiO_2–an excellent photocatalyst for degradation of organic contaminants in aqueous solution. Catal. Commun. **10**(10), 1414–1416 (2009)
10. A. Iyer et al., Nanoscale manganese oxide octahedral molecular sieves (OMS-2) as efficient photocatalysts in 2-propanol oxidation. Appl. Catal. A **375**(2), 295–302 (2010)
11. V.B.R. Boppana et al., Nanostructured alkaline-cation-containing δ-MnO_2 for photocatalytic water oxidation. Adv. Func. Mater. **23**(7), 878–884 (2013)
12. T. Gao, H. Fjellvåg, P. Norby, Structural and morphological evolution of β-MnO_2 nanorods during hydrothermal synthesis. Nanotechnology **20**(5), 055610 (2009)
13. H. Cao, S.L. Suib, Highly efficient heterogeneous photooxidation of 2-propanol to acetone with amorphous manganese oxide catalysts. J. Am. Chem. Soc. **116**(12), 5334–5342 (1994)
14. J. Chen et al., Photoassisted catalytic oxidation of alcohols and halogenated hydrocarbons with amorphous manganese oxides. Catal. Today **33**(1–3), 205–214 (1997)
15. S.R. Segal et al., Photoassisted decomposition of dimethyl methylphosphonate over amorphous manganese oxide catalysts. Chem. Mater. **11**(7), 1687–1695 (1999)
16. M. Xue et al., The direct synthesis of mesoporous structured MnO_2/TiO_2 nanocomposite: a novel visible-light active photocatalyst with large pore size. Nanotechnology **19**(18), 185604 (2008)
17. J. Zhao et al., Visible-light-driven photocatalytic degradation of ciprofloxacin by a ternary Mn_2O_3/Mn_3O_4/MnO_2 valence state heterojunction. Chem. Eng. J. **353**, 805–813 (2018)
18. Q. Zhang et al., Roles of manganese oxides in degradation of phenol under UV-Vis irradiation: adsorption, oxidation, and photocatalysis. J. Environ. Sci. **23**(11), 1904–1910 (2011)
19. S.K. Maji et al., Synthesis, characterization and photocatalytic activity of α-Fe_2O_3 nanoparticles. Polyhedron **33**(1), 145–149 (2012)
20. T.K. Tseng et al., A review of photocatalysts prepared by sol-gel method for VOCs removal. Int. J. Mol. Sci. **11**(6), 2336–2361 (2010)
21. T.O. Fufa, A.T.M.O.P. Yadav, Synthesis, characterization and photocatalytic activity of MnO_2/Al_2O_3/Fe_2O_3 nanocomposite for phenol degradation. Synthesis **6**(10) (2014)
22. S. Shukla et al., Synthesis and characterization of highly crystalline polyaniline film promising for humid sensor. Adv. Mater. Lett. **1**, 129–134 (2010)
23. G. Lövestam et al., Considerations on a definition of nanomaterial for regulatory purposes. Joint Research Centre (JRC) Reference Reports, 2010: pp. 80004–1
24. X. Wang et al., Recycling application of waste Li–MnO_2 batteries as efficient catalysts based on electrochemical lithiation to improve catalytic activity. Green Chemistry **20**, 4901 (2018)
25. A. Eslami, M. Hashemi, F. Ghanbari, Degradation of 4-chlorophenol using catalyzed peroxymonosulfate with nano-MnO_2/UV irradiation: toxicity assessment and evaluation for industrial wastewater treatment. J. Clean. Prod. **195**, 1389–1397 (2018)
26. S. Elbasuney, Dispersion characteristics of dry and colloidal nano-titania into epoxy resin. Powder Technol. **268**, 158–164 (2014)
27. K. Byrappa, S. Ohara, T. Adschiri, Nanoparticles synthesis using supercritical fluid technology—towards biomedical applications. Adv. Drug Deliv. Rev. **60**(3), 299–327 (2008)
28. S. Elbasuney, S.F. Mostafa, Continuous flow formulation and functionalization of magnesium di-hydroxide nanorods as a clean nano-fire extinguisher. Powder Technol. **278**, 72–83 (2015)
29. M.A. Elsayed, M. Gobara, S. Elbasuney, Instant synthesis of bespoke nanoscopic photocatalysts with enhanced surface area and photocatalytic activity for wastewater treatment. J. Photochem. Photobiol., A **344**, 121–133 (2017)
30. S. Elbasuney, H.E. Mostafa, Synthesis and surface modification of nanophosphorous-based flame retardant agent by continuous flow hydrothermal synthesis. Particuology **22**, 82–88 (2015)
31. S. Elbasuney et al., Stabilized super-thermite colloids: a new generation of advanced highly energetic materials. Appl. Surf. Sci. **419**, 328–336 (2017)
32. J. Li, *Engineering Nanoparticles in Near-critical and Supercritical Water* (Nottingham, University of Nottingham, 2008)
33. J.A. Darr, M. Poliakoff, New directions in inorganic and metal-organic coordination chemistry in supercritical fluids. Chem. Rev. **99**(2), 495–541 (1999)
34. T. Adschiri, Y. Hakuta, K. Arai, Hydrothermal synthesis of metal oxide fine particles at supercritical conditions. Ind. Eng. Chem. Res. **39**(12), 4901–4907 (2000)
35. T. Adschiri, K. Kanazawa, K. Arai, Rapid and continuous hydrothermal synthesis of boehmite particles in subcritical and supercritical water. Am. Ceram. Soc. **75**(9), 2615–2618 (1992)
36. S. Elbasuney, Surface engineering of layered double hydroxide (LDH) nanoparticles for polymer flame retardancy. Powder Technol. **277**, 63–73 (2015)
37. S. Elbasuney, Novel colloidal nanothermite particles (MnO_2/Al) for advanced highly energetic systems. J. Inorg. Organomet. Polym. Mater. 28(5), 1793–1800 (2018)
38. M. Elsayed, P. Hall, M. Heslop, Preparation and structure characterization of carbons prepared from resorcinol-formaldehyde resin by CO_2 activation. Adsorption **13**(3–4), 299–306 (2007)
39. S. Elbasuney, Sustainable steric stabilization of colloidal titania nanoparticles. Appl. Surf. Sci. **409**, 438–447 (2017)

40. S. Jana et al., Synthesis of superparamagnetic β-MnO_2 organosol: a photocatalyst for the oxidative phenol coupling reaction. Inorg. Chem. **47**(13), 5558–5560 (2008)
41. K. Kai et al., Room-temperature synthesis of manganese oxide monosheets. J. Am. Chem. Soc. **130**(47), 15938–15943 (2008)
42. T. Dang et al., Bio-silica coated with amorphous manganese oxide as an efficient catalyst for rapid degradation of organic pollutant. Colloids Surf. B **106**, 151–157 (2013)
43. J. Fei et al., Controlled preparation of MnO2 hierarchical hollow nanostructures and their application in water treatment. Adv. Mater. **20**(3), 452–456 (2008)
44. H. Chen, J. He, Facile synthesis of monodisperse manganese oxide nanostructures and their application in water treatment. J. Phys. Chem. C **112**(45), 17540–17545 (2008)
45. J. Rouquerol et al., *Adsorption by Powders and Porous Solids: Principles, Methodology and Applications* (Academic Press, Oxford, 2013)
46. V. Vimonses et al., An adsorption–photocatalysis hybrid process using multi-functional-nanoporous materials for wastewater reclamation. Water Res. **44**(18), 5385–5397 (2010)
47. N. Kumara et al., Equilibrium isotherm studies of adsorption of pigments extracted from Kuduk-kuduk (*Melastoma malabathricum* L.) pulp onto TiO_2 nanoparticles. J. Chem. (2014). https://doi.org/10.1155/2014/468975
48. P.K. Malik, Use of activated carbons prepared from sawdust and rice-husk for adsorption of acid dyes: a case study of acid yellow 36. Dyes Pigm. **56**(3), 239–249 (2003)
49. S.-H. Kim et al., Adsorption and photocatalysis kinetics of herbicide onto titanium oxide and powdered activated carbon. Sep. Purif. Technol. **58**(3), 335–342 (2008)
50. S. Wang et al., Fabrication of a novel bifunctional material of BiOI/Ag 3 VO 4 with high adsorption–photocatalysis for efficient treatment of dye wastewater. Appl. Catal. B **168**, 448–457 (2015)
51. H. Gulyas et al., Combining activated carbon adsorption with heterogeneous photocatalytic oxidation: lack of synergy for biologically treated greywater and tetraethylene glycol dimethyl ether. Environ. Technol. **34**(11), 1393–1403 (2013)
52. V.K. Garg et al., Basic dye (methylene blue) removal from simulated wastewater by adsorption using Indian Rosewood sawdust: a timber industry waste. Dyes Pigm. **63**(3), 243–250 (2004)
53. Y. Bulut, H. Aydın, A kinetics and thermodynamics study of methylene blue adsorption on wheat shells. Desalination **194**(1–3), 259–267 (2006)
54. J. Wei et al., MnO_2 spontaneously coated on carbon nanotubes for enhanced water oxidation. Chem. Commun. **50**(80), 11938–11941 (2014)
55. S. Li et al., Influence of MnO_2 on the photocatalytic activity of P-25 TiO_2 in the degradation of methyl orange. Sci. China Ser. B **51**(2), 179–185 (2008)
56. A.R. Sorge et al., Decomposition of hydrogen peroxide on MnO2/TiO2 catalysts. J. Propul. Power **20**(6), 1069–1075 (2004)
57. R. Ullah, J. Dutta, Photocatalytic degradation of organic dyes with manganese-doped ZnO nanoparticles. J. Hazard. Mater. **156**(1), 194–200 (2008)
58. Y.L. Chan et al. Photocatalytic degradation of rhodamine B using MnO_2 and ZnO nanoparticles. in *Materials Science Forum*, vol 756 (Trans Tech Publications, 2013), pp. 167–174
59. K. Barrett, M. McBride, Oxidative degradation of glyphosate and aminomethylphosphonate by manganese oxide. Environ. Sci. Technol. **39**(23), 9223–9228 (2005)
60. G. Li et al., 2,4,5-Trichlorophenol degradation using a novel TiO_2-coated biofilm carrier: roles of adsorption, photocatalysis, and biodegradation. Environ. Sci. Technol. **45**(19), 8359–8367 (2011)
61. S. Lan et al., Hierarchical hollow structure ZnO: synthesis, characterization, and highly efficient adsorption/photocatalysis toward Congo red. Ind. Eng. Chem. Res. **53**(8), 3131–3139 (2014)
62. L. Zhang et al., Synthesis of a thin-layer MnO_2 nanosheet-coated Fe_3O_4 nanocomposite as a magnetically separable photocatalyst. Langmuir **30**(23), 7006–7013 (2014)
63. R. Jothiramalingam, M. Wang, Synthesis, characterization and photocatalytic activity of porous manganese oxide doped titania for toluene decomposition. J. Hazard. Mater. **147**(1), 562–569 (2007)
64. V.B.R. Boppana, F. Jiao, Nanostructured MnO_2: an efficient and robust water oxidation catalyst. Chem. Commun. **47**(31), 8973–8975 (2011)
65. Y. He et al., Synthesis of MnO_2 nanosheets on montmorillonite for oxidative degradation and adsorption of methylene blue. J. Colloid Interface Sci. **510**, 207–220 (2018)
66. B. Xing et al., Preparation of TiO_2/activated carbon composites for photocatalytic degradation of RhB under UV light irradiation. J. Nanomater. **2016**, 3 (2016)